THE JOURNAL OF PHYSICAL CHEMISTRY C
A JOURNAL OF THE AMERICAN CHEMICAL SOCIETY

pubs.acs.org/JPCC

Article

Tracking Lithiation of Si-Based Anodes in Real Time by Total Scattering Computed Tomography

David S. Wragg,* Casper Skautvedt, Anders Brennhagen, Carina Geiß, Stefano Checchia, and Alexey Y. Koposov*

Cite This: *J. Phys. Chem. C* 2023, 127, 23149–23155

Read Online

ACCESS | Metrics & More | Article Recommendations | Supporting Information

ABSTRACT: The existing set of characterization tools does not permit a full description of the three-dimensional (3D) structure and operating mechanisms of amorphous, low-scattering alloying active materials in metal-ion batteries. In this article, we describe and demonstrate a new methodology for analysis of this class of materials based on total scattering computed tomography. Using silicon (Si)-based anodes as a testing platform, we can not only visualize the chemical changes taking place in the electrodes during lithiation but also create a 3D mapping of the electrode components including amorphous active and inactive materials. The mapping was used to select a region of interest in the electrode from which the best possible *operando* pair distribution function (PDF) of the active material could be obtained. Finally, we deployed differential analysis to highlight the small but systematic changes in the PDF during lithiation, revealing subtle structural transformations at the atomic scale.

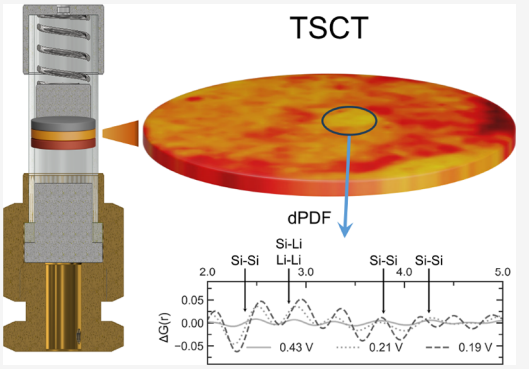

INTRODUCTION

The continuing improvement of modern metal-ion batteries strongly depends on the development of active materials with increased charge capacity. Graphite has been used as the main active component in Li-ion battery (LIB) anodes since their commercialization in 1991.[1] A theoretical maximum Li-ion storage capacity of 372 mAh g^{-1}, from one Li- ion per six carbon atoms, is a limiting factor for improvements in battery performance.[2] Materials with an alloying mechanism can store substantially more Li^+ per formula unit. Silicon (Si), the most promising example, can host up to 4.4 Li ions per Si atom, leading to a theoretical capacity of 4200 mAh g^{-1}. A similar scenario is observed for Na-ion batteries (NIBs), where hard carbon is currently the anode material of choice, but alloying materials (such as P, Sn, Sb, and others) offer greater capacities.[3] Although these anode materials have an astonishing potential to improve the energy density of metal-ion batteries, their cycling stability remains a major barrier to commercial implementation.

To improve the performance of alloying materials in metal-ion batteries, it is crucial to fully understand the operation and degradation mechanisms that lead to structural and morphological changes and, as a result, to a rapid loss of capacity during cycling. The nature of the changes that occur during cycling of alloying anodes (volume changes, cracking, and void formation) means that it is advantageous to consider changes in both the atomic and microscopic structure of the anode. Many attempts have been made over the years to establish a reliable methodology for such characterization at various scales,[4,5] but the set of techniques that can be used is limited by several factors: (i) amorphization almost always occurs during initial cycling; (ii) the most promising materials have low molecular weight, giving excellent gravimetric capacity but low X-ray scattering power and ruling out most X-ray spectroscopic methods[6]; and (iii) amorphization of the starting material is a common method for extending the cycle life of alloying anode materials. Most of the characterization to date has been performed *ex situ* (or post-mortem), i.e., after the electrochemical cell has been disassembled and the materials removed for analysis. This allows both relaxation of the chemistry and contamination through exposure to an external environment different from that inside the cell.[7]

Operando studies, where the structure of the materials and electrochemistry of the battery cell are probed simultaneously under working conditions, provide the most realistic information on the chemical processes taking place in the cell.[7−9] However, specially designed cells are required for *operando* measurements, and it is not always possible to perfectly reproduce the electrochemical performance of conventional cells.

Received: September 25, 2023
Revised: November 2, 2023
Accepted: November 3, 2023
Published: November 22, 2023

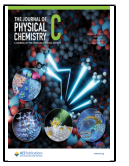

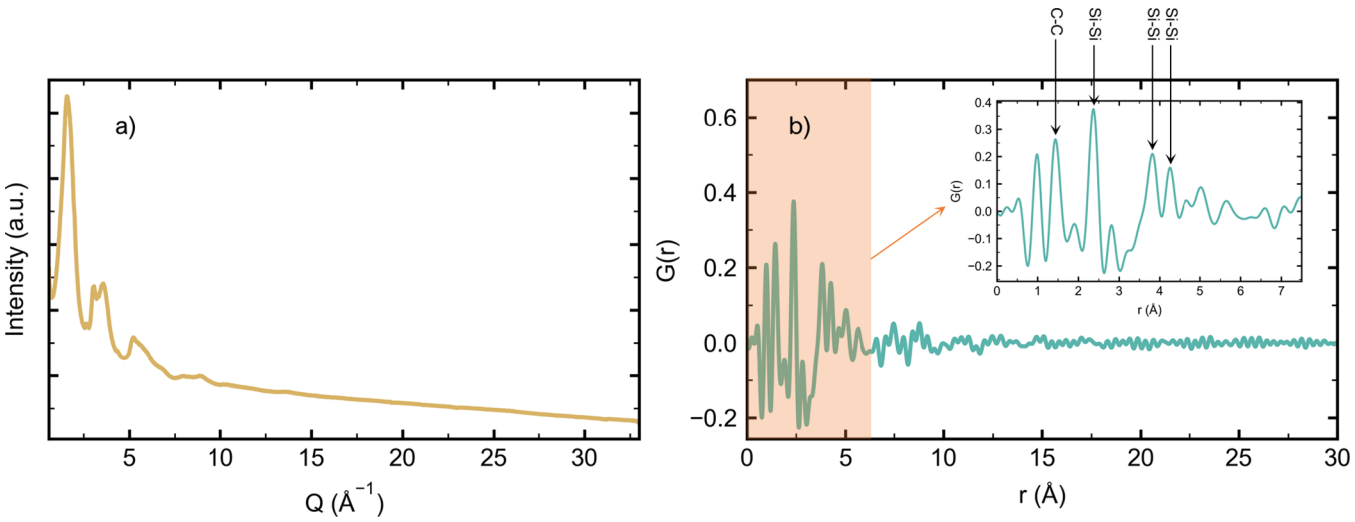

Figure 1. (a) XRD ($I(Q)$) pattern for the first scan showing the pattern of an electrode prepared from amorphous Si in the Q-range from 0 to 36 Å^{-1} vs the intensity of the signal. (b) Area-averaged PDF ($G(r)$) of the Si-based electrode showing the lack of long-range order. The inset shows the peak assignments.

X-ray diffraction (XRD) methods, which are typically used to characterize inorganic solids used in LIB and NIB anodes, are largely blind to the amorphous parts of a sample. A related and more suitable method for studying amorphous materials is total scattering, usually analyzed as the pair distribution function (PDF).[10] This method uses the signal underneath the Bragg peaks to obtain information about the local structure, enabling the characterization of amorphous materials if background contributions are properly subtracted. PDF analysis has become a key tool for understanding LIB and NIB anode materials that undergo amorphization during cycling. Furthermore, *operando* PDF is an excellent method for studying active battery materials that are amorphous from the start.[11,12] However, for weakly scattering, amorphous materials such as Si and P contributions from other components in typical *operando* cells (mostly designed for XRD or spectroscopy) are usually much stronger than the signal from the active electrode. As a result, challenges related to the subtraction of background and scattering from cell components other than the active electrode (Li or Na counter electrodes, Al/Cu-foil, cell windows, *etc.*) have limited the number of successful studies to date. Typically, these are also single-point measurements.

We have developed total scattering computed tomography (TSCT) as a method for *operando* battery studies, capable of mapping the sample in 3D and selectively obtaining high-quality data on the active electrodes without the need for subtraction of background or signals from other battery components. TSCT is a development of X-ray diffraction computed tomography (XRDCT), which has been used extensively for *operando* studies of catalysts, fuel cells, and batteries in five dimensions (time, 3D space, and crystal structure information).[13−22] TSCT uses the same experimental methodology as XRDCT but with high X-ray energy to give data with a suitable Q-range for conversion to the atomic PDF.[23,24] The structural data can then be analyzed in either real (PDFCT) or reciprocal (XRDCT) space. The data collection required for this is more time-consuming than for XRDCT, and the PDF data from the first TSCT study could only be analyzed by averaging the entire anode area.[13] *Operando* PDFCT mapping of batteries (revealing changes in a bismuth metallate anode both at the atomic and microscopic scales) has only recently been demonstrated using data collected on a fourth-generation synchrotron beamline at the European synchrotron (ESRF).[25,26]

In this work, we further develop and demonstrate *operando* total scattering computed tomography (TSCT). Even though TSCT has enormous potential for obtaining detailed structural information from complex battery materials, it is not commonly used due to the high-quality data collection and extensive data processing required. Si provides an excellent challenge for TSCT development: it is a weak X-ray scatterer, and due to extreme volume changes during lithiation/delithiation (up to 400%), amorphization of the material occurs very quickly even for highly crystalline samples. Although *operando* studies have been carried out on Si in LIBs using various methods,[6,27−32] the most detailed atomic level structural study of the changes in the amorphous material during cycling to date comes from *ex situ* PDF data.[33−36]

We used the TSCT method to study small changes in the structure of a Si-based anode in the early stages of lithiation. The observation of a complete lithiation cycle was not possible due to the unreliable cell performance at low voltages, possibly caused by electrolyte leakage during sample transport. The initial amorphous structure of the anode allowed us to evaluate the PDFCT mapping methodology prior to *operando* measurement by identifying the signals of the anode components and mapping their distributions using XRD and PDF. We then obtained high-quality *operando* PDFs by averaging over an area where the maps showed high levels of Si active material. Even in the area-averaged PDFs, only small changes could be observed, and we applied the difference PDF (dPDF) approach to highlight and quantify the systematic structural changes during the limited lithiation possible for this cell.

METHODS

We collected *operando* TSCT data on anodes with amorphous 100 nm Si nanoparticles (for SEM micrographs showing size and diffraction data showing amorphous character, see Figures S1 and S2) prepared by silane pyrolysis[37] as the active component. Si-based LIB anodes usually contain a significant amount of graphite as a conductive additive. As the crystalline

https://doi.org/10.1021/acs.jpcc.3c06414
J. Phys. Chem. C 2023, 127, 23149−23155

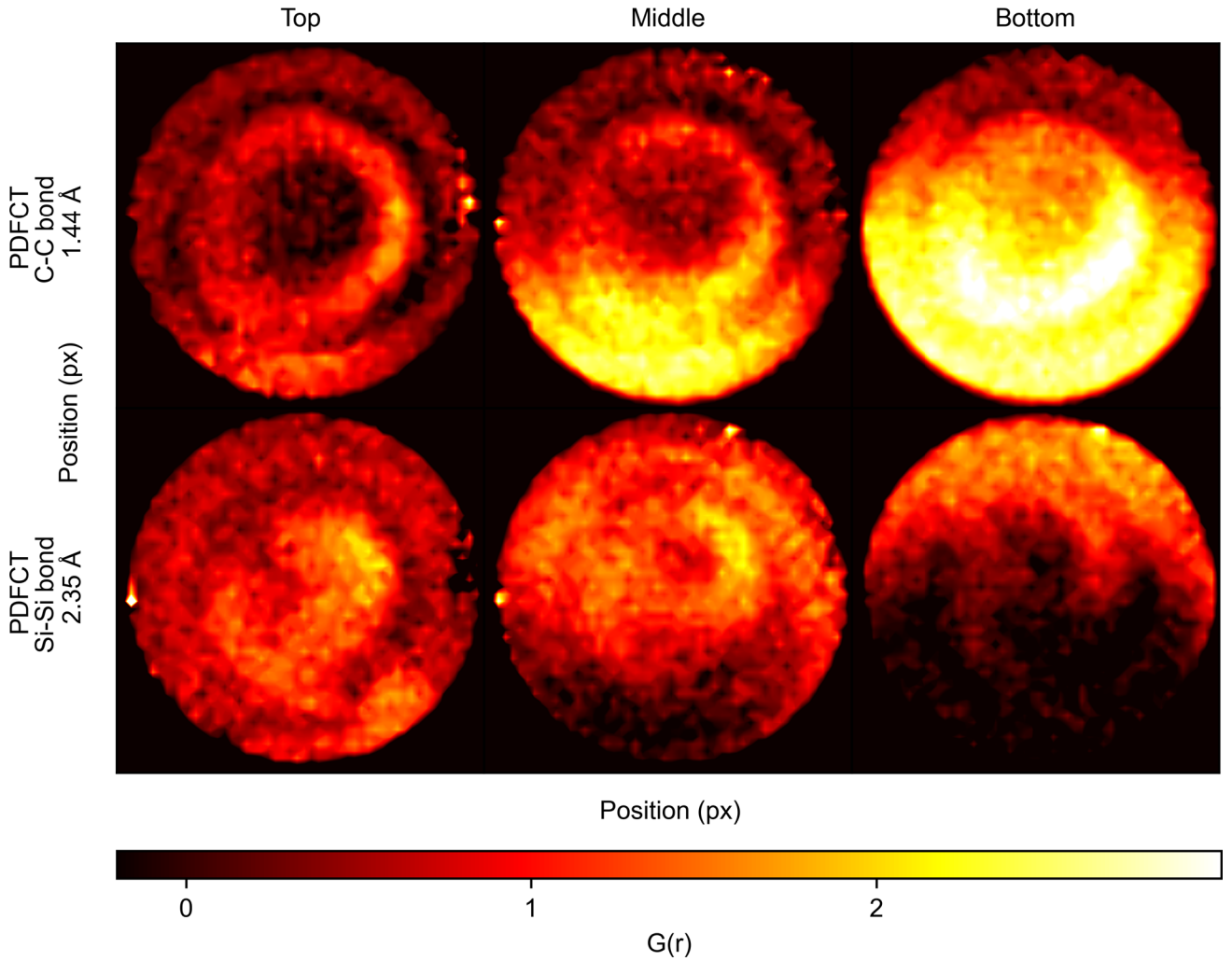

Figure 2. Comparison of PDFCT slices showing nano-Si and carbon black distributions at 0.5 V. The left scans are closest to the separator, and the right scans are closest to the glassy carbon current collector. The high carbon black intensity in the lower half of the right slice may be due to the slight misalignment of the cell, causing the beam to pass through the current collector.

structure of graphite would dominate the total scattering data, we instead used carbon black (amorphous) as a conductive additive in our electrodes. Carbon black has a very limited capacity for Li in the voltage range used.[38] The slurry composition was optimized to give an electrochemical performance similar to that of conventional Si-graphite electrodes. Full details of slurry and electrode preparation and selection, along with coin cell galvanostatic cycling results for the composition used in the *operando* experiments, are shown in the Supporting Information (Figures S3 and S4). We did not evaluate the long-term cycling of the anode composition as the *operando* experiment was focused on studying the initial cycles. The TSCT cell was based on our earlier designs, and the arrangement of battery components inside it is shown and described in detail in the Supporting Information (Figure S5).[25] TSCT data were collected at beamline ID15A of the ESRF. The data collection, reconstruction, and PDF conversion methods are described in the Supporting Information.

RESULTS

The first TSCT scan was carried out prior to the start of lithiation to provide a baseline and check the quality of the data. Slices were collected at three different heights in the electrode (closest to the separator, middle, and closest to the current collector). Figure 1 shows the area-averaged XRD ($I(Q)$) and corresponding PDF ($G(r)$) patterns obtained from the middle TSCT slice at the start of the experiment. The amorphous nature of Si is evident in the $I(Q)$ plot (no sharp Bragg peaks) and in the PDF plot (no visible peaks above $r \approx 6$ Å).

We assigned the peaks in the PDF based on the crystal structure of Si and previous PDF studies.[33,39] The first peak at ~1.45 Å corresponds to C−C bonds from the conductive additive (carbon black), which makes up 20% of the electrode by mass. The next peak at ~2.40 Å represents the Si−Si bond with a possible small contribution from the cross-ring distances in carbon black. This is slightly longer than the expected length of 2.35 Å, reported in the literature.[40] The small discrepancy could be a result of the amorphous nature of the Si nanoparticles used for electrode preparation. Residual hydrogen, often present in Si particles obtained through silane pyrolysis, may also affect the average Si−Si bond distance.[41] In general, however, the PDF appears similar to the *ex situ* PDFs of Si/C anode composites reported previously by Key et al. and Ulvestad et al.[33,42] The peak at a physically meaningless

https://doi.org/10.1021/acs.jpcc.3c06414
J. Phys. Chem. C 2023, 127, 23149−23155

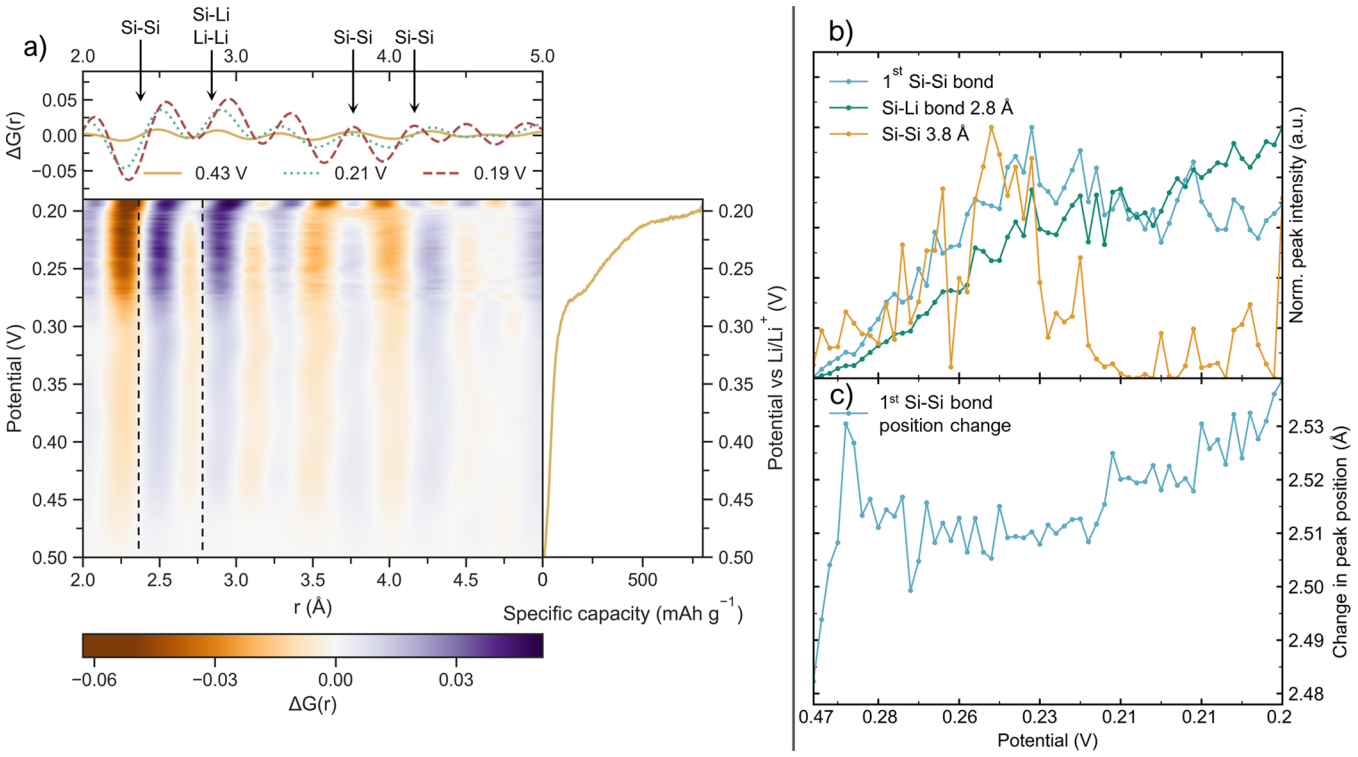

Figure 3. (a) Evolution of the dPDF for the middle slice of the Si-based electrode measured at 150 mA g^{-1} as a function of the applied electrochemical potential. dPDFs for selected potentials are plotted in one-dimension at the top to highlight the changes over time. The contour pattern below is the series of *operando* dPDFs, (b) normalized dPDF peak intensities vs potential, and (c) position of the dPDF signal from extension of the first Si−Si bond vs potential. Note that the *x* axes (potential) in panels (b) and (c) are nonlinear and shared.

distance of 1 Å is caused by the truncation of the Fourier transform, which converts the scattering data to a PDF, due to the limited *Q*-range in the TSCT data.

The peaks corresponding to Si−Si bond distances from the second and third coordination shells can be found at 3.80 and 4.20 Å, respectively. The peaks appearing at higher *r*-values are comparable to the noise and therefore cannot be properly assigned, which is expected for an amorphous sample.

The first two peaks in the area-averaged PDF (∼1.45 and ∼2.40 Å; see Figure S6) are strong enough to be obvious in the PDFs of individual voxels (Figure S7) and, therefore, can be used to map the distribution of the conductive additive (carbon black) and active material (Si) in the electrode. Figure 2 shows reconstructed PDFCT slice maps at the start of lithiation at three different heights (the left panel represents the vertical position closest to the separator, the middle panel is approximately the middle of the active electrode, and the right panel represents the closest to the current collector), giving the distributions of Si and carbon black in 3D, with resolutions of 130 μm in *x* and *y* (slice dimensions) and 25 μm in *z* (slice height).

Generally, Si seems to be more concentrated in the center of the electrode slices and closer to the top (cell separator). This may be somewhat affected by the cell alignment in the plane of the beam (see below). The ring-like patterns seen in the distributions of both Si and carbon black in the PDFCT may be caused by uneven slurry distribution during the electrode casting processes or the pressure inside the cell. The distribution of amorphous carbon also suggests an imperfect alignment of the cell in the plane of the X-ray beam. The very high levels of carbon in the lower half of the maps for the middle and bottom slices are probably caused by the X-ray beam passing through the part of the glassy carbon piston current collector underneath the active electrode, which has a structure similar to carbon black. The lack of overlap between the Si and C distributions in Figure 2 suggests that the contribution of carbon black to the PDF intensity at $G(r) = 2.4$ Å is limited.

The analysis described above reveals the distribution of the active and inactive components in the electrode. This information is potentially useful for optimization of the electrode processing as redistribution of the materials can occur during drying.[43]

The maps shown in Figure 2 are used to select the region of interest containing a high concentration of active material. Area-averaged PDFs from a circle of a 16-voxel radius, centered 1 voxel below and 3 voxels right of the center, in the middle slices for the whole series of tomograms, were used to analyze the changes in the Si material during the *operando* experiment. Unfortunately, we were unable to fully lithiate the anode during the *operando* experiment, and we only have data over the range 0.50−0.20 V vs Li/Li^+. The low level of lithiation resulting from this means that the changes in the PDF with the state of charge are very small (see Figure S8); however, using the dPDF approach recently described by Stratford et al., small but systematic changes are observed.[44] To obtain the dPDF, we simply subtract the first PDF in the lithiation series from the subsequent ones to highlight the differences. Figure 3a shows a 2D film plot of the dPDF during the *operando* experiment (see also Figure S9). To further clarify the trends, we fitted the squared intensity and position of the dPDF peaks throughout the *operando* data series using TOPAS v6 (the fitting procedure is described in the Supporting Information, Figures S10 and S11).[45] The results

https://doi.org/10.1021/acs.jpcc.3c06414
J. Phys. Chem. C 2023, 127, 23149−23155

for the intensities of the signals at ~2.5 Å (extension of the Si−Si direct bond), 2.8 Å (Si−Li direct bond),[33,46] and 3.8 Å (second shell Si−Si distance) are shown in Figure 3b, while the variation in the position of the signal corresponding to the extension of the first Si−Si bond peak is shown in Figure 3c. Variations in the dPDF below 2 Å are not related to Si−Si or Si−Li bonds, and variations around the 1.44 Å C−C bond length (as well as a peak at 1.8 Å) appear to have only a weak correlation with the electrochemistry, although there is a possibility that some completely new peaks may appear in this region due to the rapid buildup of a solid electrolyte interface/interphase on the silicon electrode surface. It is likely that most of the dPDF peaks below 2 Å are dominated by truncation noise due to the limited *Q*-range of the TSCT data.

The first clear change, increasing intensity in all of the significant dPDF peaks, starts around 0.48 V *vs* Li/Li^+, which corresponds well with the first plateau in the lithiation curve (Figure S4). The next apparent development, a steep increase in intensity of the Si−Li peak at ~2.8 Å, occurs at 0.28 V *vs* Li/Li^+, corresponds to the second lithiation plateau. At the same time, the 2D dPDF plot (Figure 3a) shows a clear loss of intensity at 2.25 Å with a corresponding increase at around 2.5 Å (Figure 3c). This represents the elongation of the Si−Si bonds due to lithiation.

The final electrochemical plateau around 0.21 V *vs* Li/Li^+ sees the peak at 3.8 Å (second shell Si−Si interactions) start to decrease. At the same time, the Si−Si peak, now centered around 2.4 Å, continues to shift toward higher *r* as Si−Si bonds stretch and the long-range structure begins to disintegrate.

DISCUSSION

The changes observed in the *operando* dPDF confirm the previous PDF results from Key et al. where crystalline Si was studied at different stages of cycling by *ex situ* PDF measurements. Since our data is based on amorphous Si, the results described by Key et al. for the second discharge[33] (at which point the Si is fully amorphous) are the most relevant comparison for our experiment. The PDF peaks in which we observed significant variation above were assigned according to this work.

The changes observed by Key et al. between PDF data points at 0.26 and 0.20 V *vs* Li/Li^+ in the second lithiation show the same pattern in peak position that we observe between 0.50 and 0.20 V *vs* Li/Li^+: a slight shift of the 2.35 Å peak to higher *r* (lithiation extending the Si−Si bond). At lower voltage, the 2.8 Å Si−Li peak also increases in intensity, and the 3.8 Å second shell Si−Si peak disappears. This may correspond to the loss of long-range order in the particles with clusters of more than four to five silicon atoms breaking down. These changes are hard to detect in the two *ex situ* data points that cover a voltage range comparable to our *operando* experiment.[33] Our *operando* data set shows that these changes, although small, are part of a continuous transition that corresponds to the electrochemical changes. Figure 3b,c shows that the *operando* dPDF results also allow us to determine the potentials at which the structural changes occur with a good level of precision.

Some of the changes we observe in the dPDF data could conceivably be related to the lithiation of the carbon black additive; however, we believe that this is not a likely explanation for several reasons: (i) carbon black represents only 20% of the anode composition by weight, (ii) it has limited lithiation capacity in this voltage range, (iii) the appearance of the 2.8 Å peak assigned to Si−Li (by Key et al.[33]) and this study does not correspond to any C−Li or C−C bonding interaction, which we would expect to appear during lithiation, and (iv) full lithiation of carbon black has a very small effect on its PDF peaks.[25]

CONCLUSIONS

We have demonstrated TSCT as a method for mapping the 3D distribution of weakly scattering, amorphous active (Si), and inactive (carbon black) materials in a LIB anode. The generated 3D maps allowed us to select an area of the anode with the highest Si concentration and use it to monitor the atomic-level structural changes during lithiation. dPDF analysis of area-averaged PDFs selected from this region revealed extremely subtle changes at the early stages of lithiation, i.e., formation of Si−Li bonding, elongation of the Si−Si bonds, and possible loss of longer range Si−Si interactions. The *operando* dPDF data obtained by averaging areas in the PDFCT tomograms enabled us to determine when these chemical changes occured with much better precision than the existing *ex situ* studies: initial structural changes begin at 0.48 V *vs* Li/Li^+, while the major lithiation process starts at 0.28 V *vs* Li/Li^+. These results illustrate the ability of this technique to accurately determine what chemical reactions are happening at which point during cycling, even for very subtle changes in the structure of weak and amorphous X-ray scatters like Si.

ASSOCIATED CONTENT

Supporting Information

The Supporting Information is available free of charge at https://pubs.acs.org/doi/10.1021/acs.jpcc.3c06414.

Experimental details related to the cell fabrication, measurements, and cell design (PDF)

AUTHOR INFORMATION

Corresponding Authors

David S. Wragg − *Centre for Material Science and Nanotechnology, Department of Chemistry, University of Oslo, Oslo 0371, Norway; Department of Battery Technology, Institute for Energy Technology (IFE), Kjeller 2027, Norway;* orcid.org/0000-0001-8502-7912; Email: david.wragg@ife.no

Alexey Y. Koposov − *Centre for Material Science and Nanotechnology, Department of Chemistry, University of Oslo, Oslo 0371, Norway; Department of Battery Technology, Institute for Energy Technology (IFE), Kjeller 2027, Norway;* orcid.org/0000-0001-5898-3204; Email: alexey.koposov@kjemi.uio.no

Authors

Casper Skautvedt − *Centre for Material Science and Nanotechnology, Department of Chemistry, University of Oslo, Oslo 0371, Norway;* orcid.org/0000-0002-4521-3080

Anders Brennhagen − *Centre for Material Science and Nanotechnology, Department of Chemistry, University of Oslo, Oslo 0371, Norway;* orcid.org/0000-0003-4467-6750

Carina Geiß − *Centre for Material Science and Nanotechnology, Department of Chemistry, University of Oslo, Oslo 0371, Norway*

Stefano Checchia − *European Synchrotron Radiation Facility (ESRF), Grenoble 38043, France*

Complete contact information is available at: https://pubs.acs.org/10.1021/acs.jpcc.3c06414

Author Contributions

D.S.W.: experiment design, writing, conceptualization, revising, analyzing, data processing, and data collection. C.S.: writing, analyzing, revising, visualization, data processing, sample characterization, and conceptualization. A.B.: data collecting, revising, writing, and analyzing. C.G.: sample preparation and writing. S.C.: data processing and data collection. A.Y.K.: writing, conceptualization, revising, and analyzing.

Notes

The authors declare no competing financial interest.

■ ACKNOWLEDGMENTS

This work was performed with the support of MoZEES, a Norwegian Centre for Environment-Friendly Energy Research (FME), cosponsored by the Research Council of Norway (project number 257653). We thank the ESRF for access to beamline ID15A through experiment number ch-5682 and acknowledge the use of the Norwegian National Infrastructure for X-ray Diffraction and Scattering (RECX, Norwegian Research Council project number: 208896)

■ REFERENCES

(1) Lu, Y.; Zhang, Q.; Chen, J. Recent progress on lithium-ion batteries with high electrochemical performance. *Science China Chemistry* **2019**, *62* (5), 533−548.

(2) Eshetu, G. G.; Zhang, H.; Judez, X.; Adenusi, H.; Armand, M.; Passerini, S.; Figgemeier, E. Production of high-energy Li-ion batteries comprising silicon-containing anodes and insertion-type cathodes. *Nat. Commun.* **2021**, *12* (1), 5459.

(3) Hasa, I.; Mariyappan, S.; Saurel, D.; Adelhelm, P.; Koposov, A. Y.; Masquelier, C.; Croguennec, L.; Casas-Cabanas, M. Challenges of today for Na-based batteries of the future: From materials to cell metrics. *J. Power Sources* **2021**, *482*, No. 228872.

(4) McDowell, M. T.; Lee, S. W.; Nix, W. D.; Cui, Y. 25th Anniversary Article: Understanding the Lithiation of Silicon and Other Alloying Anodes for Lithium-Ion Batteries. *Adv. Mater.* **2013**, *25* (36), 4966−4985.

(5) Balke, N.; Jesse, S.; Kim, Y.; Adamczyk, L.; Tselev, A.; Ivanov, I. N.; Dudney, N. J.; Kalinin, S. V. Real Space Mapping of Li-Ion Transport in Amorphous Si Anodes with Nanometer Resolution. *Nano Lett.* **2010**, *10* (9), 3420−3425.

(6) Masahiro, O.; Shigekazu, O.; Takeshi, A.; Toyonari, Y.; Toshiaki, O. Operando Analysis of Silicon Anode for Lithium Ion Battery Using Soft X-ray Absorption Spectroscopy. *JFE Tech. Rep.* **2023**, *27*, 16−20.

(7) Liu, D.; Shadike, Z.; Lin, R.; Qian, K.; Li, H.; Li, K.; Wang, S.; Yu, Q.; Liu, M.; Ganapathy, S.; et al. Review of Recent Development of In Situ/Operando Characterization Techniques for Lithium Battery Research. *Adv. Mater.* **2019**, *31* (28), No. 1806620.

(8) Brennhagen, A.; Cavallo, C.; Wragg, D. S.; Sottmann, J.; Koposov, A. Y.; Fjellvåg, H. Understanding the (De)Sodiation Mechanisms in Na-Based Batteries through Operando X-Ray Methods. *Batteries & Supercaps* **2021**, *4* (7), 1039−1063.

(9) Gourdin, G.; Doan-Nguyen, V. In situ, operando characterization of materials for electrochemical devices. *Cell Reports Physical Science* **2021**, *2* (12), No. 100660.

(10) Egami, T.; Billinge, S. J. L. *Underneath the Bragg peaks: structural analysis of complex materials*, 2nd ed.; Pergamon materials series; Elsivier: Pergamon, 2012.

(11) Allan, P. K.; Griffin, J. M.; Darwiche, A.; Borkiewicz, O. J.; Wiaderek, K. M.; Chapman, K. W.; Morris, A. J.; Chupas, P. J.; Monconduit, L.; Grey, C. P. Tracking Sodium-Antimonide Phase Transformations in Sodium-Ion Anodes: Insights from Operando Pair Distribution Function Analysis and Solid-State NMR Spectroscopy. *J. Am. Chem. Soc.* **2016**, *138* (7), 2352−2365.

(12) Chapman, K. W. Emerging operando and x-ray pair distribution function methods for energy materials development. *MRS Bull.* **2016**, *41* (3), 231−240.

(13) Sottmann, J.; Di Michiel, M.; Fjellvåg, H.; Malavasi, L.; Margadonna, S.; Vajeeston, P.; Vaughan, G. B. M.; Wragg, D. S. Chemical Structures of Specific Sodium Ion Battery Components Determined by Operando Pair Distribution Function and X-ray Diffraction Computed Tomography. *Angew. Chem., Int. Ed.* **2017**, *56* (38), 11385−11389.

(14) Vamvakeros, A.; Jacques, S. D. M.; Di Michiel, M.; Matras, D.; Middelkoop, V.; Ismagilov, I. Z.; Matus, E. V.; Kuznetsov, V. V.; Drnec, J.; Senecal, P.; et al. 5D operando tomographic diffraction imaging of a catalyst bed. *Nat. Commun.* **2018**, *9* (1), 4751.

(15) Liu, H.; Kazemiabnavi, S.; Grenier, A.; Vaughan, G.; Di Michiel, M.; Polzin, B. J.; Thornton, K.; Chapman, K. W.; Chupas, P. J. Quantifying Reaction and Rate Heterogeneity in Battery Electrodes in 3D through Operando X-ray Diffraction Computed Tomography. *ACS Appl. Mater. Interfaces* **2019**, *11* (20), 18386−18394.

(16) Finegan, D. P.; Vamvakeros, A.; Cao, L.; Tan, C.; Heenan, T. M. M.; Daemi, S. R.; Jacques, S. D. M.; Beale, A. M.; Di Michiel, M.; Smith, K.; et al. Spatially Resolving Lithiation in Silicon−Graphite Composite Electrodes via in Situ High-Energy X-ray Diffraction Computed Tomography. *Nano Lett.* **2019**, *19* (6), 3811−3820.

(17) Li, T.; Heenan, T. M. M.; Rabuni, M. F.; Wang, B.; Farandos, N. M.; Kelsall, G. H.; Matras, D.; Tan, C.; Lu, X.; Jacques, S. D. M.; et al. Design of next-generation ceramic fuel cells and real-time characterization with synchrotron X-ray diffraction computed tomography. *Nat. Commun.* **2019**, *10* (1), 1497.

(18) Finegan, D. P.; Vamvakeros, A.; Tan, C.; Heenan, T. M. M.; Daemi, S. R.; Seitzman, N.; Di Michiel, M.; Jacques, S.; Beale, A. M.; Brett, D. J. L.; et al. Spatial quantification of dynamic inter and intra particle crystallographic heterogeneities within lithium ion electrodes. *Nat. Commun.* **2020**, *11* (1), 631.

(19) Tonin, G.; Vaughan, G. B. M.; Bouchet, R.; Alloin, F.; Di Michiel, M.; Barchasz, C. Operando investigation of the lithium/sulfur battery system by coupled X-ray absorption tomography and X-ray diffraction computed tomography. *J. Power Sources* **2020**, *468*, No. 228287.

(20) Wragg, D. S.; Kalantzopoulos, G. N.; Pappas, D. K.; Pinilla-Herrero, I.; Rojo-Gama, D.; Redekop, E.; Di Michiel, M.; Beato, P.; Lundegaard, L. F.; Svelle, S. Mapping the coke formation within a zeolite catalyst extrudate in space and time by operando computed X-ray diffraction tomography. *J. Catal.* **2021**, *401*, 1−6.

(21) Matras, D.; Vamvakeros, A.; Jacques, S. D. M.; di Michiel, M.; Middelkoop, V.; Ismagilov, I. Z.; Matus, E. V.; Kuznetsov, V. V.; Cernik, R. J.; Beale, A. M. Multi-length scale 5D diffraction imaging of Ni−Pd/CeO2−ZrO2/Al2O3 catalyst during partial oxidation of methane. *Journal of Materials Chemistry A* **2021**, *9* (18), 11331−11346.

(22) Heenan, T. M. M.; Mombrini, I.; Llewellyn, A.; Checchia, S.; Tan, C.; Johnson, M. J.; et al. Mapping internal temperatures during high-rate battery applications. *Nature* **2023**, *617* (7961), 507−512.

(23) Jacques, S. D. M.; Di Michiel, M.; Kimber, S. A. J.; Yang, X.; Cernik, R. J.; Beale, A. M.; Billinge, S. J. L Pair distribution function computed tomography. *Nat. Commun.* **2013**, *4* (1), 2536.

(24) Jensen, K. M. Ø.; Aluri, E. R.; Perez, E. S.; Vaughan, G. B. M.; Di Michel, M.; Schofield, E. J.; Billinge, S. J. L.; Cussen, S. A. Location and characterization of heterogeneous phases within Mary Rose wood. *Matter* **2022**, *5* (1), 150−161.

(25) Sottmann, J.; Ruud, A.; Fjellvåg, Ø. S.; Vaughan, G. B. M.; Di Michel, M.; Fjellvåg, H.; Lebedev, O. I.; Vajeeston, P.; Wragg, D. S.5D total scattering computed tomography reveals the full reaction mechanism of a bismuth vanadate lithium ion battery anode. *Phys. Chem. Chem. Phys.* **2022**, *24* (44), 27075−27085.

(26) Vaughan, G. B. M.; Baker, R.; Barret, R.; Bonnefoy, J.; Buslaps, T.; Checchia, S.; Duran, D.; Fihman, F.; Got, P.; Kieffer, J.; et al.

ID15A at the ESRF - a beamline for high speed operando X-ray diffraction, diffraction tomography and total scattering. *Journal of Synchrotron Radiation* **2020**, *27* (2), 515−528.
(27) Li, J.; Dahn, J. R. An In Situ X-Ray Diffraction Study of the Reaction of Li with Crystalline Si. *J. Electrochem. Soc.* **2007**, *154* (3), A156.
(28) Ogata, K.; Salager, E.; Kerr, C. J.; Fraser, A. E.; Ducati, C.; Morris, A. J.; Hofmann, S.; Grey, C. P. Revealing lithium−silicide phase transformations in nano-structured silicon-based lithium ion batteries via in situ NMR spectroscopy. *Nat. Commun.* **2014**, *5* (1), 3217.
(29) Pietsch, P.; Hess, M.; Ludwig, W.; Eller, J.; Wood, V. Combining operando synchrotron X-ray tomographic microscopy and scanning X-ray diffraction to study lithium ion batteries. *Sci. Rep.* **2016**, *6* (1), 27994.
(30) Vanpeene, V.; King, A.; Maire, E.; Roué, L. In situ characterization of Si-based anodes by coupling synchrotron X-ray tomography and diffraction. *Nano Energy* **2019**, *56*, 799−812.
(31) Choi, P.; Parimalam, B. S.; Su, L.; Reeja-Jayan, B.; Litster, S. Operando Particle-Scale Characterization of Silicon Anode Degradation during Cycling by Ultrahigh-Resolution X-ray Microscopy and Computed Tomography. *ACS Applied Energy Materials* **2021**, *4* (2), 1657−1665.
(32) Krotkov, D.; Schneier, D.; Menkin, S.; Horowitz, Y.; Peled, E.; Golodnitsky, D.; Fleischer, S. Operando Terahertz Spectroscopy of Solid Electrolyte Interphase Evolution on Silicon Anodes. *Batteries & Supercaps* **2022**, *5* (1), No. e202100183.
(33) Key, B.; Morcrette, M.; Tarascon, J.-M.; Grey, C. P. Pair Distribution Function Analysis and Solid State NMR Studies of Silicon Electrodes for Lithium Ion Batteries: Understanding the (De)lithiation Mechanisms. *J. Am. Chem. Soc.* **2011**, *133* (3), 503−512.
(34) Alves Dalla Corte, D.; Caillon, G.; Jordy, C.; Chazalviel, J.-N.; Rosso, M.; Ozanam, F. Spectroscopic Insight into Li-Ion Batteries during Operation: An Alternative Infrared Approach. *Adv. Energy Mater.* **2016**, *6* (2), No. 1501768.
(35) Chen, C.; Oudenhoven, J. F. M.; Danilov, D. L.; Vezhlev, E.; Gao, L.; Li, N.; Mulder, F. M.; Eichel, R.-A.; Notten, P. H. L. Origin of Degradation in Si-Based All-Solid-State Li-Ion Microbatteries. *Adv. Energy Mater.* **2018**, *8* (30), No. 1801430.
(36) Glazer, M. P. B.; Cho, J.; Almer, J.; Okasinski, J.; Braun, P. V.; Dunand, D. C. In Operando Strain Measurement of Bicontinuous Silicon-Coated Nickel Inverse Opal Anodes for Li-Ion Batteries. *Adv. Energy Mater.* **2015**, *5* (14), No. 1500466.
(37) Lai, S. Y.; Mæhlen, J. P.; Preston, T. J.; Skare, M. O.; Nagell, M. U.; Ulvestad, A.; Lemordant, D.; Koposov, A. Y. Morphology engineering of silicon nanoparticles for better performance in Li-ion battery anodes. *Nanoscale Advances* **2020**, *2* (11), 5335−5342.
(38) Fransson, L.; Eriksson, T.; Edström, K.; Gustafsson, T.; Thomas, J. O. Influence of carbon black and binder on Li-ion batteries. *J. Power Sources* **2001**, *101* (1), 1−9.
(39) Kyushin, S.; Kurosaki, Y.; Otsuka, K.; Imai, H.; Ishida, S.; Kyomen, T.; Hanaya, M.; Matsumoto, H. Silicon−silicon π single bond. *Nat. Commun.* **2020**, *11* (1), 4009.
(40) Hom, T.; Kiszenik, W.; Post, B. Accurate lattice constants from multiple reflection measurements II. lattice constants of germanium, silicon and diamond Locality: synthetic Sample: at T = 25 C. *J. Appl. Crystallogr.* **1975**, *8*, 457−458.
(41) Legesse, M.; Nolan, M.; Fagas, G. A first principles analysis of the effect of hydrogen concentration in hydrogenated amorphous silicon on the formation of strained Si-Si bonds and the optical and mobility gaps. *J. Appl. Phys.* **2014**, *115*, 20.
(42) Ulvestad, A.; Skare, M. O.; Foss, C. E.; Krogsæter, H.; Reichstein, J. F.; Preston, T. J.; Mæhlen, J. P.; Andersen, H. F.; Koposov, A. Y. Stoichiometry-Controlled Reversible Lithiation Capacity in Nanostructured Silicon Nitrides Enabled by in Situ Conversion Reaction. *ACS Nano* **2021**, *15* (10), 16777−16787.
(43) Hawley, W. B.; Li, J. Electrode manufacturing for lithium-ion batteries—Analysis of current and next generation processing. *Journal of Energy Storage* **2019**, *25*, No. 100862.
(44) Stratford, J. M.; Kleppe, A. K.; Keeble, D. S.; Chater, P. A.; Meysami, S. S.; Wright, C. J.; Barker, J.; Titirici, M.-M.; Allan, P. K.; Grey, C. P. Correlating Local Structure and Sodium Storage in Hard Carbon Anodes: Insights from Pair Distribution Function Analysis and Solid-State NMR. *J. Am. Chem. Soc.* **2021**, *143* (35), 14274−14286.
(45) Coelho, A. TOPAS and TOPAS-Academic: an optimization program integrating computer algebra and crystallographic objects written in C++. *J. Appl. Crystallogr.* **2018**, *51* (1), 210−218.
(46) Kim, H.; Kweon, K. E.; Chou, C.-Y.; Ekerdt, J. G.; Hwang, G. S. On the Nature and Behavior of Li Atoms in Si: A First Principles Study. *J. Phys. Chem. C* **2010**, *114* (41), 17942−17946.

https://doi.org/10.1021/acs.jpcc.3c06414
J. Phys. Chem. C 2023, 127, 23149−23155